An automatic algorithm for detecting stent endothelialization from volumetric optical coherence tomography datasets

**Garret T Bonnema[1], Kristen O'Halloran Cardinal[2,5],
Stuart K Williams[3,5] and Jennifer K Barton[1,4]**

[1] The College of Optical Sciences, The University of Arizona, Tucson, AZ, USA
[2] Biomedical and General Engineering, California Polytechnic State University, USA
[3] Cardiovascular Innovation Institute, The University of Louisville, Louisville, KY 40292, USA
[4] Biomedical Engineering, The University of Arizona, Tucson, AZ, USA
[5] Research performed at the University of Arizona.

Abstract
Recent research has suggested that endothelialization of vascular stents is crucial to reducing the risk of late stent thrombosis. With a resolution of approximately 10 μm, optical coherence tomography (OCT) may be an appropriate imaging modality for visualizing the vascular response to a stent and measuring the percentage of struts covered with an anti-thrombogenic cellular lining. We developed an image analysis program to locate covered and uncovered stent struts in OCT images of tissue-engineered blood vessels. The struts were found by exploiting the highly reflective and shadowing characteristics of the metallic stent material. Coverage was evaluated by comparing the luminal surface with the depth of the strut reflection. Strut coverage calculations were compared to manual assessment of OCT images and epi-fluorescence analysis of the stented grafts. Based on the manual assessment, the strut identification algorithm operated with a sensitivity of 93% and a specificity of 99%. The strut coverage algorithm was 81% sensitive and 96% specific. The present study indicates that the program can automatically determine percent cellular coverage from volumetric OCT datasets of blood vessel mimics. The program could potentially be extended to assessments of stent endothelialization in native stented arteries.

(Some figures in this article are in colour only in the electronic version)

1. Introduction

Studies have established that approximately 10–20% of patients treated with bare metal stents require secondary procedures due to restenosis (Fischman *et al* 1994, Salam *et al* 2006, Serruys *et al* 1994). To address restenosis associated with bare metal stents, drug eluting stents have been developed that exhibit anti-proliferative and/or anti-inflammatory action to reduce the hyperplastic response following device deployment (Salam *et al* 2006). However, suppressing the vessel response may lead to a different problem, namely drug-eluting stents inhibiting the formation of a protective endothelial cell lining. Studies suggest the exposed stent–strut surface may serve as a nidus for thrombus formation (Finn *et al* 2007). Late stent thrombosis (LST) associated with drug-eluting stents has been noted in several studies (Iakovou *et al* 2005, Pfisterer *et al* 2006). Different stent designs and drugs can induce unique responses from the arterial wall (Finn *et al* 2007, Konig *et al* 2002, Taylor *et al* 2001) and have different risks for LST. During histological examination of autopsy specimens, stents associated with LST often show reduced endothelial coverage (Farb *et al* 2002, Finn *et al* 2007). In a study of morphometric predictors, Finn *et al* (2007) demonstrated that the ratio of uncovered to total struts was the best predictor of LST.

Intravascular ultrasound (IVUS) and optical coherence tomography (OCT) are two imaging modalities that may be used to indirectly assess LST risk *in vivo* by evaluating recellularization of strut surfaces. Researchers have used ultrasound to monitor the neointimal volume (Suzumura *et al* 2002) and length of the stent that was free from intimal hyperplasia (Mintz *et al* 2005). Echogenic contrast agents have been used to improve measurements of the neointimal area (Masuda *et al* 2001). Although appropriate for vessels with significant neointimal hyperplasia, IVUS systems may not have adequate resolution to detect stent endothelialization (Matsumoto *et al* 2007, Mintz *et al* 2005). Researchers have demonstrated an improvement in both resolution and dynamic range for optical coherence tomography in comparison to commercial IVUS systems (Brezinski 2006, Brezinski *et al* 1997). With approximately 10 μm axial resolution, this depth-resolved imaging modality is capable of visualizing both neointimal hyperplasia and the thin cellular lining associated with stent endothelialization (Bouma *et al* 2003, Buellesfeld *et al* 2005, Ito *et al* 2005, Kume *et al* 2005, Matsumoto *et al* 2007, Takano *et al* 2007, Tanigawa *et al* 2007).

Volumetric scans with OCT promise better measures of endothelialization of the stent surface. However, the time-intensive nature of image analysis is a major limitation for using large image sets to assess strut endothelialization. An algorithm has been developed to automatically detect covered and uncovered struts and establish a percent cellular coverage for a volumetric OCT dataset.

To develop and test the algorithm, a tissue-engineered blood vessel was used as an *in vitro* model of human blood vessels. Although these blood vessel mimics (BVMs) do not have the blood constituents and adventitia of a native artery, they have been shown to model the intimal response to a deployed stent (Cardinal *et al* 2006). BVMs provide an excellent platform for development of imaging techniques and image processing algorithms prior to expensive and time-consuming animal studies. Previous work has demonstrated the utility of OCT for visualizing the BVM cellular lining and the feasibility of monitoring its response to deployed metal stents (Bonnema *et al* 2007). The aims of the current study were to (1) visualize the response of blood vessel mimics to deployed stents using OCT, (2) calculate percent cellular coverage for each stent using an automatic algorithm and (3) compare the algorithm results to other measures of strut coverage including manual calculations from OCT images and *en face* fluorescent staining.
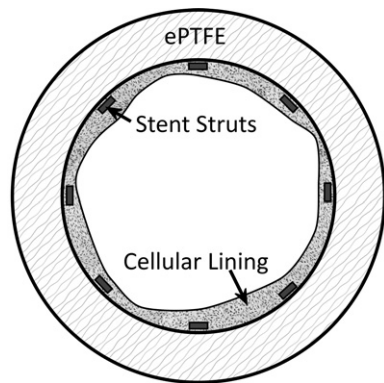
Figure 1. Cross-sectional schematic of a stented blood vessel mimic.

2. Experimental methods

2.1. The blood vessel mimics

As described by Cardinal *et al* (2006), the blood vessel mimic (BVM) is a tissue engineered blood vessel that consists of a polymeric scaffold and a luminal cell lining. The polymeric scaffold provides the mechanical support and a biocompatible surface for the cellular lining of the BVM. For these experiments, 4.0 mm inner diameter, expanded polytetrafluoroethylene (ePTFE) tubing (Impra Bard, Inc., Tempe, AZ) was used as the scaffold material. Microvascular endothelial cells were extracted from human adipose tissue. After processing, the cells were pressure sodded onto the lumen of the BVM and developed within a bioreactor. The bioreactors have been described previously (Cardinal *et al* 2006). Briefly, the bioreactor consists of three components: (1) a peristaltic pump, (2) a chamber containing the BVM and (3) a media reservoir. The peristaltic pump delivers nutrient-rich media to the developing mimic that is located in the BVM chamber. The media reservoir is used to facilitate the exchange of media during the development of the mimic. Similar to *in vivo* blood vessels, devices such as stents can be deployed in the BVM using sterile introducing catheters. A cross-sectional view of a stented BVM is shown schematically in figure 1.

2.2. The OCT system

The OCT system and endoscope have been described previously (Bonnema *et al* 2007). This time-domain OCT system consisted of a 1300 nm superluminescent diode with a 100 nm bandwidth. The axial point spread function was measured to be 10 μm in air. A rapid scanning Fourier-domain optical delay line was used to achieve acquisition rates from 100 to 1000 axial scans (a-scans) per second. Because image acquisition in these mimics was not time critical all OCT images were acquired at a relatively slow 200 a-scans s^{-1}. The sample arm consisted of a miniature endoscope which could be introduced into the lumen of the BVM and could acquire longitudinal images at any angle within the mimic. The optics of the miniature endoscope provided a lateral resolution of 20 μm at a working distance of 400 μm outside the endoscope window. A sterile glass cover was placed over the endoscope to prevent contamination of the developing mimic during imaging.

2.3. Experiments

Twelve BVMs were developed and imaged with OCT before and after the deployment of a vascular stent. After 7 days of development within the bioreactor, either a bare metal or protein-modified stent was deployed within each mimic. To further modulate the cellular response, half of the mimics containing each type of stent were developed using a greater media flow rate. The two flow rates were 15 and 60 mL min^{-1}.

OCT images were acquired of the BVMs immediately pre- and post-stenting to assess whether a cellular lining was present and to monitor stent deployment characteristics such as stent apposition and possible dissection of the cellular lining. The BVMs were additionally imaged at 3, 7, 14 and 20 days post-stent deployment. Each image was 15 mm long by 2 mm deep assuming a refractive index of 1.33. Each image consisted of 3000 pixels in the longitudinal and 625 pixels in the depth directions. A total of 12 images were collected from a stented BVM at each time point.

At day 20, the BVMs were removed from the bioreactor and fixed in 3% gluteraldehyde. Ten of the twelve mimics were imaged volumetrically with OCT while submerged in the fixation agent. Four hundred, equally spaced longitudinal images were acquired from around the circumference of the mimic. Each image was 8 mm long (800 pixels) and 2 mm deep (625 pixels). A lower sampling resolution was used to minimize the memory requirements for the volumetric data set. After volumetric imaging, eight of the ten mimics were prepared for histology or BBI fluorescence, and the additional two mimics were fixed and saved for future optical studies such as confocal microscopy.

3. Image analysis software

A MATLAB program was developed to automatically identify all struts in the OCT image and further tag those struts that were covered by >30 μm thickness of cellular material. The program consisted of three main components: (1) defining the strut search region by identifying the luminal surface of the BVM and excluding artifactual a-scans; (2) identifying struts based on their bright surface reflection, dark shadow and concentrated intensity; and (3) identifying covered struts based on distance between the BVM luminal surface and the bright strut surface reflection. The program was executed using a graphical user interface for ease of use. An overall flow chart for the program is shown in figure 2, and each component is described in more detail below.

3.1. Step 1: defining the strut search region

The strut search region was narrowed to avoid the confounding effects of BVM connectors and debris. To identify the luminal surface of the BVM, an iterative approach was used. First, the maximum reflected intensity in each a-scan was determined. Then, the shallowest pixel in each a-scan that exceeded half the maximum intensity was located. This operation provided a rough estimate of the luminal surface. However, the estimated surface profile was often located within the BVM rather than at the true surface. Therefore, a small number of pixels (65) luminal to the estimated surface was analyzed. The shallowest pixel in this region that exceeded 20% of the maximum a-scan intensity was recorded. This operation correctly identified the true surface across the majority of the BVM. However, saturation artifacts over highly reflective metallic struts led to sharp discontinuities in the surface profile. These erroneous data points were eliminated by using a running median filter with a kernel size of 31 pixels on the surface profile.
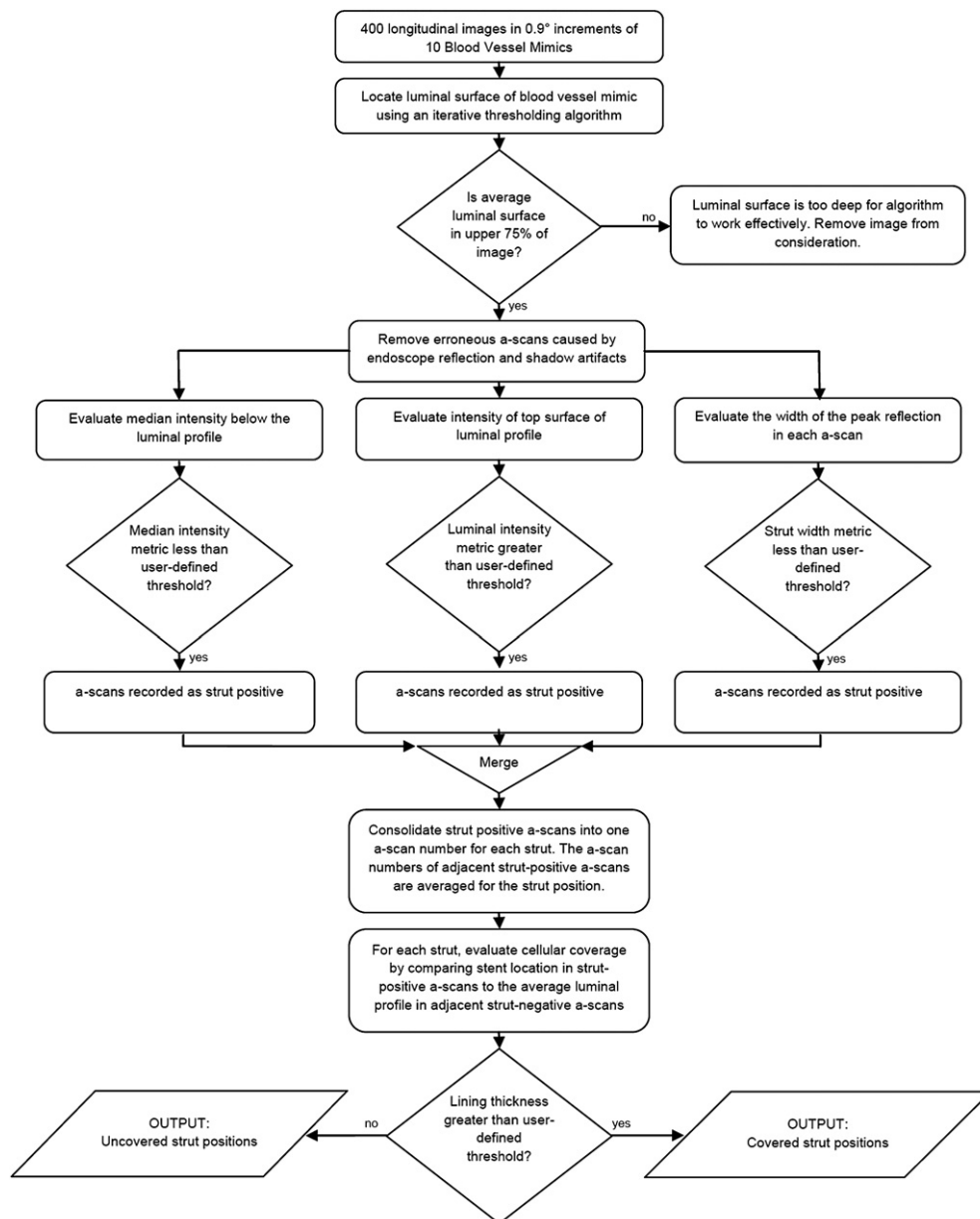
Figure 2. The basic execution of the strut identification software. An OCT image was analyzed using three metrics to identify the struts. An additional algorithm was developed to determine whether the identified struts were covered with a cellular lining.

Non-strut-associated dark shadows and bright reflections were caused by debris and by the connectors holding the BVM in the bioreactor chamber. The MATLAB program automatically identified these two situations and removed the associated a-scans from further analysis. To eliminate shadowed regions caused by debris on the endoscope window or within the culture media, a maximum intensity of each a-scan was calculated. An intensity less than
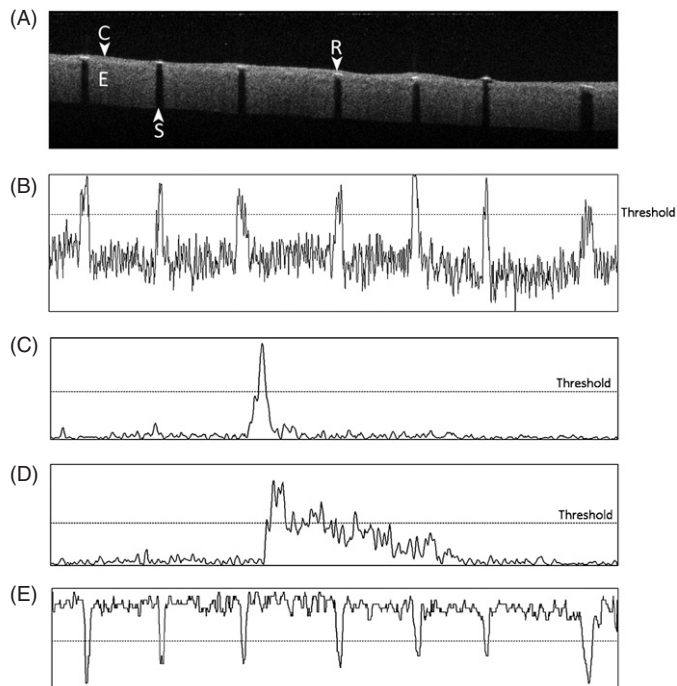
Figure 3. The strut reflection metric evaluates the maximum reflected intensity in each a-scan. (A) An example OCT image of a stented blood vessel mimic: C, cellular lining; E, ePTFE scaffold; S, strut shadow; R, strut reflection. (B) The strut reflection metric. The threshold is based on the average intensity and a user-specified number of standard deviations of the most luminal 50 μm of the mimic. The intensity profile of a strut-positive a-scan (C) exhibits a rapid rise and fall in intensity with depth compared to a strut-negative a-scan (D). (E) The median metric. The threshold is based on the metric mean and a user-specified number of standard deviations of the metric. The image size is 8 mm × 2 mm.

a user-defined number of standard deviations from the average (for this analysis, set at 3) was indicative of a shadow artifact. To eliminate the connector regions, the program evaluated the calculated profile for large, discontinuous jumps that were associated with the edge of the plastic connector. A jump in the profile greater than 10 pixels indicated the location of the connector edge. The side of this edge with the shallower profile was identified as the connector. The positions of affected a-scans were recorded so that they would be excluded from the later analysis.

3.2. Step 2: locating stent struts

Struts were identified based on three defining image characteristics: a bright reflection at the surface of the strut, concentrated energy (that is, a rapid rise then fall in intensity for strut-positive a-scans) and a dark shadow underneath the strut. Not every strut exhibited all of these characteristics, but after defining the appropriate search region in step 1, it was rare for non-strut regions to exhibit any of them. Therefore, a strut was identified if it met any one of these criteria. A more detailed explanation for each characteristic follows.

Metallic struts were usually associated with reflections that were bright relative to the average intensity of the BVM. An example of this appearance is shown in figure 3. A maximum
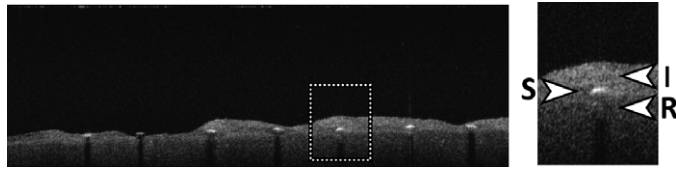
Figure 4. A detailed view of a covered strut shows the typical visualization: S, luminal strut reflection; I, cellular lining from incident light; R, cellular lining from strut-reflected light. The left image is 5 mm × 2 mm.

intensity metric (MIM) was designed that would be sensitive to this bright reflection. First, median filtering was performed with a 3 × 3 pixel kernel to remove single pixel noise. Using the luminal surface profile found in step 1, the overall mean and standard deviation of the intensity were calculated for the shallowest 50 μm of the BVM. The maximum intensity value for each a-scan was also calculated. A threshold was set as the mean plus a user-defined number of standard deviations. This number was defined as the 'strut reflection parameter'. If the maximum a-scan intensity value exceeded the threshold, the a-scan was recorded as a MIM strut positive. An example OCT image and its corresponding maximum a-scan intensity metric are shown in figures 3(A) and (B), respectively.

A complementary algorithm utilizing the intensity profile of the a-scan was developed to increase sensitivity. As shown in figure 3(C), a characteristic of the strut-positive a-scans is a more rapid rise and fall in intensity with depth than the strut-negative a-scans (figure 3(D)). To quantify this observation, the maximum pixel intensity was found for each a-scan of the original unfiltered image. The number of pixels with intensities greater than half the maximum intensity (the full-width, half-maximum or FWHM) was calculated. The vector containing a-scan FWHM values for the entire image was then smoothed with a one-dimensional running median filter with a kernel size of 11 pixels, to eliminate erroneous false positives from single a-scans (true struts were a minimum of eight a-scans wide). Since approximately 65% of struts were identified using MIM criteria, the strut-positive a-scans identified during that process provided an appropriate basis for automatic determination of the FWHM metric threshold. Any a-scan with a FWHM less than the average of the MIM strut-positive a-scans was also marked as strut-positive.

The final characteristic that defined struts was dark vertical shadows below the strut surface. To automatically detect this image attribute, a metric was developed that evaluated the median pixel intensities beneath the luminal surface. Prior to analysis, histogram equalization was performed on the image to increase the local contrast between the ePTFE scaffold and the shadow caused by the metallic strut. Linearization of the pixel intensity cumulative distribution function typically increased the difference between the shadow and scaffold pixel intensities. The highly reflective metallic struts caused the signal above the strut to appear to be mirrored beneath the strut. For struts covered by a cellular lining, this effect resulted in the most luminal pixels of the strut shadow being displaced by a distance approximately equal to the thickness of the cellular lining. This effect is shown in figure 4. The difference between the mimic luminal profile and the position of the maximum pixel intensity served as an estimate for the cellular lining thickness (i.e. the difference between the position of the mimic surface and the strut surface). For each a-scan, the median intensity of the 50 pixels deeper than the luminal profile plus twice this estimated thickness was calculated (the 'shadow median intensity metric' (SMIM)). A threshold was set using the mean of the SMIM minus a user-specified number of standard deviations of the metric. This number of
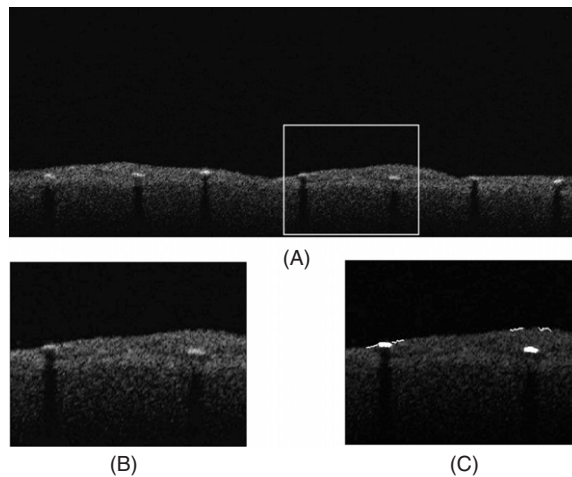
Figure 5. The cell coverage algorithm determines whether a strut is covered with cellular material by comparing the position of the strut to the position of the luminal surface. (A) A stented BVM with both covered and uncovered struts. (B) An enlarged section showing a covered and uncovered strut. (C) The algorithm finds the average axial position of the luminal profile adjacent to the strut-positive a-scans, indicated with a thin white line. The profile position is compared to the position of the strut, indicated with a thick line. A strut is covered if the distance between these two positions exceeds a user-defined threshold. The image in (C) has been darkened to emphasize strut and profile indicators. Image A is 7.8 mm ×2.0 mm. Images B and C are 2.0 mm × 1.0 mm.

standard deviations was defined as the 'strut shadow parameter'. As shown in figure 3, those a-scans that had a SMIM less than the threshold value were recorded as strut-positive.

3.3. Step 3: determining cellular coverage

To determine cellular coverage, an algorithm was developed to evaluate the difference between the luminal profile of the mimic and the position of the luminal strut surface. The high reflectivity of the metallic strut would often saturate the detection electronics resulting in a broadening of the axial point spread function. This artifact would occasionally result in inaccurate locations of the mimic luminal surface immediately above the struts. Because of this inaccuracy, the luminal profile of the mimic (the top of the cellular lining) over a strut was defined by averaging the position at adjacent sides. The position of the strut surface was determined by averaging the positions of the maximum pixel intensity in contiguous strut positive a-scans. The difference between these two positions was calculated, and if this difference exceeded a user-defined threshold (defined as the 'cell coverage parameter'), the strut was identified as covered. Figure 5 shows an OCT image containing both covered and uncovered struts, and illustrates the step in identifying the covered strut.

4. Image analysis methodology

Image analysis was performed in three steps. First, the total number of images was reduced to facilitate analysis. Poor quality images associated with deep luminal surfaces were also removed. Second, a training set of randomly selected images was used to determine the

optimal parameters for the automated algorithm. Third, each image was evaluated by both the algorithm and three observers. These steps are described in detail below.

4.1. Removal of images

Prior to any analysis, images were removed from consideration. For volumetric datasets, each image was separated by $0.9°$. It was determined by visual inspection that very little change in the strut distribution and cellular coverage occurred between adjacent images. Therefore, there was no need to evaluate each of the 400 images per BVM. Every other image was removed from consideration such that each analyzed image was separated by $1.8°$.

Additional images were removed if the average depth of the BVM luminal surface profile was within the bottom quarter of the image, or out of the field of view of the OCT system. The low contrast and poor lateral resolution associated with these deep surfaces rendered image analysis difficult. This criterion was evaluated by the program such that the removal of these poor images was performed automatically without any user intervention. The position of the luminal surface was based on the orientation of the BVM with respect to the endoscope and was independent of the cellular coverage of the struts. This step reduced the total number of images from 2000 to 1461.

4.2. Evaluation of the training set

To determine optimal parameters for the automated algorithm, a training set of 150 images was randomly selected from the total number of 1461 images. A sample size of 150 images was found to display similar statistics as larger sample sizes. Three observers evaluated each of the training images. With assistance from a custom MATLAB program with a graphical user interface, each observer recorded the locations of covered and uncovered struts for each image. Statistical measures of sensitivity, specificity and percent correct classification (positive predictive value) were calculated for the automated strut identification and cell coverage algorithms using the observer data as the gold standard. The statistical measures based on each of the three observers were then averaged for a final estimate of the performance. Strut identification and cell coverage parameters were varied to find optimum values. The strut identification parameters that provided equal sensitivity and a percent correct classification rate were chosen. The cell coverage parameter was selected to provide a high percent correct classification rate while maximizing sensitivity. This optimized set of parameters was then used universally for the comprehensive analysis of the ten BVMs.

Several assumptions and approximations were made to calculate statistical performance measures for the 150-image dataset. First, the strut identification results had no well-defined true negative. An estimate of the number of true negatives was obtained by dividing the total number of strut-negative a-scans by the average strut width in each image. This method produced a large number of true negatives that resulted in high values for specificity. Second, a wide strut was often identified to be multiple struts by the algorithm. These wide reflections occurred when imaging near cross-members where the strut reflection could be up to 750 μm wide, compared to the average width of 80 μm. Since these multiple algorithm-identified strut-positive regions correspond to an actual strut, they were considered true positives in the statistical analysis. A third assumption was made for thin struts located in close proximity to each other. This occurred near junctions and notches at cross-members of the stent. The algorithm occasionally identified the two adjacent struts as a wide continuous strut. Since both adjacent struts are associated with an algorithm-identified region, those two struts were counted as one true positive. This assumption was implemented for observer-identified struts
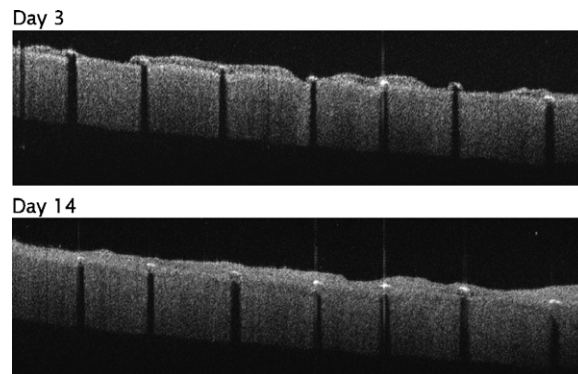
Figure 6. Two OCT images taken from the same approximate location in a stented mimic at 3 and 14 days post-deployment.

separated by less than 100 μm, where the normal separation between struts was on the order of 1 mm.

4.3. Evaluation of complete datasets

A manual analysis was performed to calculate percent cellular coverage for the ten BVMs. Three observers blind to the BVM development conditions viewed each of the 1461 images in random order. Each observer recorded the number of struts covered by cellular material and the total number of struts in every image. An average observer-based percent cellular coverage was calculated for each of the BVMs. These average measurements served as the gold standard.

The automated algorithm evaluated the same 1461 images using the optimal parameter set determined from the 150-image training set. The automatic results were compared with the observational measurements of the 1461 images and results from bisbenzimide (BBI) fluorescence analysis. A single blinded observer evaluated the BBI images and assigned a score from 1 to 5 based on the following criteria:

1 = little to no cell coverage
2 = some cells interspersed on the stent surface
3 = subconfluent cell coverage with localized areas of cell density
4 = confluent cell coverage
5 = highest density of cell coverage on the stent surface

The Pearson product–moment correlation coefficient was calculated for the percent cellular coverage OCT calculations and the BBI analysis.

5. Results

Example OCT images taken at 3 and 14 days post-stent deployment are shown in figure 6. The 3 days' image shows incomplete cellular coverage of the struts with a relatively hypointense cellular lining. By day 14, this portion of the BVM exhibits a confluent cellular lining, which is also more hyperintense. Visual inspection of all OCT images taken during bioreactor development of the BVMs showed that in general these trends held for all BVMs—the coverage became more confluent and the lining became more hyperintense over time.
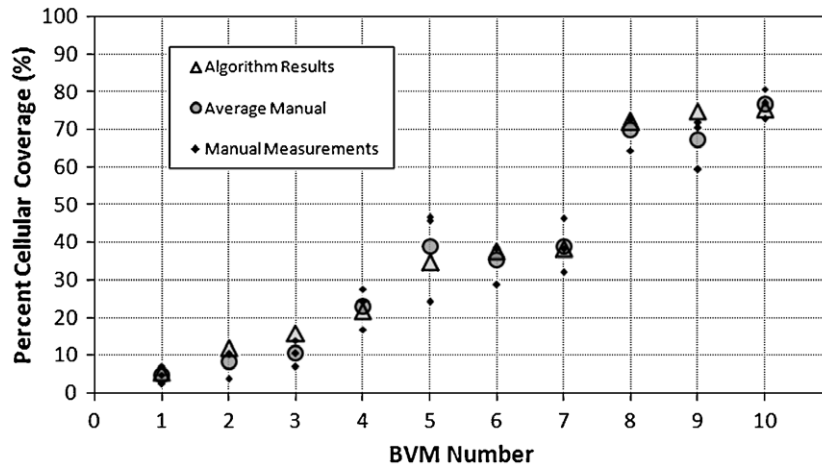
Figure 7. Comparison between percent cellular coverage determined by observers and the algorithm.

Table 1. The results from the strut analysis algorithm.

ID	Number of images	Algorithm results (%)	Average observer results (%)	BBI score
1	137	5.5	4.7	2.50
2	166	12.1	8.2	2.25
3	108	16.4	10.4	2.63
4	181	21.7	23.0	3.00
5	172	34.8	38.9	3.75
6	133	37.7	35.4	–
7	146	38.3	38.9	3.63
8	174	72.2	70.0	3.67
9	139	75.3	67.2	–
10	149	75.7	76.9	4.38

Excellent results were obtained applying the automated algorithm to the 20 days post-stent deployment volumetric datasets. Using the training set, a strut reflection parameter of 4.0 and a strut shadow parameter of 3.1 were chosen to balance the sensitivity and correct classification rate of the strut identification algorithms. These parameters provided a strut identification sensitivity of 93%, a specificity of 99% and a correct classification rate (positive predictive value, PPV) of 95%. The cellular coverage parameter was 9 pixels. This parameter provided a sensitivity of 81% and a specificity of 96%. The cellular coverage algorithm had a correct classification rate (PPV) of 95%.

The parameters chosen based on the 150-image training set were then used to evaluate the ten volumetric datasets. The average image analysis time was approximately 500 ms per image. The algorithm-determined percent cellular coverage for each of the ten analyzed blood vessel mimics are displayed in table 1, along with the average observer-determined percent cellular coverage and the BBI score. A graphical comparison between the observational and algorithm percent cellular coverage measurements is shown in figure 7. On average, the
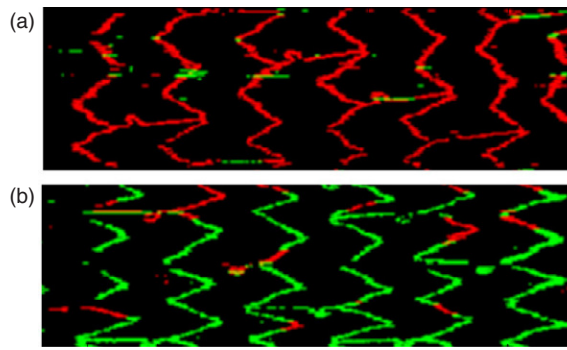
Figure 8. Stent maps for two different blood vessel mimics showing the locations of covered (green) and uncovered (red) struts.

algorithm predicted a 1.6% greater cellular coverage compared to the observer measurements. The largest difference between the algorithm and average observer measurements was 8.1%.

Figure 8 shows a mapping of the strut surface for a bare metal (top) and protein modified (bottom) stent in two blood vessel mimics developed at the lower flow rate. These images were created by first unfolding the tubular volumetric data set such that rotation $0°$ is at the top of the image and rotation $358.2°$ is at the bottom, then flattening the volume by assigning each a-scan a color: black = no strut, red = uncovered strut and green = covered strut as determined by the automated algorithm.

6. Discussion

OCT clearly visualized the temporal response of the BVM to a deployed stent, as illustrated in figure 6. On average, the thickness of the cellular lining increased with time after stenting and the lining became more hyperintense. The increase in intensity may result from a greater concentration of scatterers located within the cellular lining. Previous research has shown that scattering in tissue occurs due to intracellular organelles (e.g. mitochondria, nuclei) rather than the size and shape of the overall cells (Mourant *et al* 1998). Increases in the concentration of nuclei and mitochondria may be increasing the backscattered intensity of the lining. Further time-serial studies examining OCT images and corresponding histological sections are required to definitively explain this increase in lining intensity.

The strut identification algorithms provided excellent sensitivity, specificity and PPV (93%, 99% and 95%, respectively). The cellular coverage algorithm provided excellent PPV (95%) but only moderate sensitivity (81%). The results of the cellular coverage algorithm could be modulated by the choice of the cell coverage parameter. For example, the cell coverage parameter could be chosen such that it (1) balanced sensitivity and specificity, (2) balanced sensitivity and percent correct classification or (3) produced the greatest distance from the no discrimination line in the receiver operator characteristic curve. Using the 150-image dataset, we chose to balance the tradeoff between sensitivity and percent correct classification for the cell coverage parameter. As shown in figure 9, the upper limit on percent correct classification was approximately 93%. A cell coverage parameter of 9 pixels was selected since it maintained this high percent correct classification with a large sensitivity. The point corresponding to this chosen parameter is indicated with a square in a plot of sensitivity versus percent correct classification shown in figure 9.
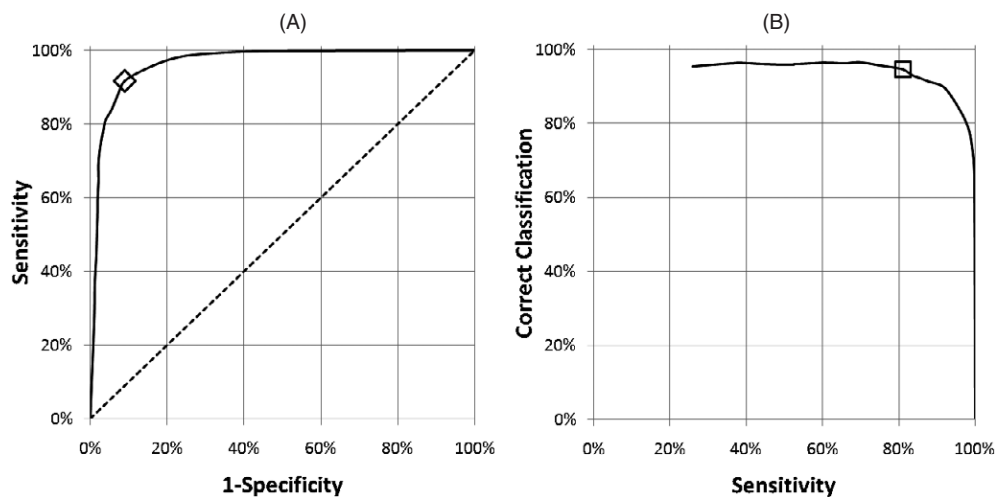
Figure 9. Performance of the cell coverage algorithm based on range of parameters. (A) The receiver operator characteristic curve. The dotted line represents the line of no discrimination. A cell coverage parameter of 6, indicated by the diamond, would provide the greatest distance from the line of no discrimination. (B) A plot of the percent correct classification versus sensitivity. A cell coverage parameter of 9, indicated by the square box, was selected because it provided a high correct classification rate with an appropriate sensitivity.

The performance of the algorithm depended on the selection of the reflection and shadow parameters. In this study, the parameters were optimized using manual analysis of randomly selected images from the ten datasets. This optimized set of parameters was then used universally for the comprehensive analysis of the ten BVMs. Although the mimics were developed under different growth conditions and exhibited a variety of responses, the algorithm performed well for each mimic suggesting that this same universal parameter set can be used in future OCT studies of stented blood vessel mimics without the need for manually evaluating additional training sets. However, the parameter set was specific to one OCT system. The parameters may require reoptimization for different OCT systems. If the algorithm is extended for the analysis of other stented vessels, such as native arteries, additional studies will be performed to determine an optimal parameter set and whether it can be used universally for all OCT datasets of native arteries.

A cell coverage parameter of 9 implies the minimum lining thickness of a covered strut identified by the algorithm was 30 μm. Although the measured resolution of the OCT system was 10 μm, bright reflections from the metallic strut occasionally saturated the detection electronics resulting in a broadened axial point spread function. This limited the ability for both the observers and the algorithm to resolve linings less than 30 μm thick. Several methods could be implemented to improve the minimum detectable lining. First, the polarization state of the incident light could be optimized to reduce the specular reflections associated with these metal surfaces. Second, an endoscope could be designed to image the struts at a shallower angle of incidence. Either design would need to carefully balance saturation prevention with the need to maintain a strong reflection in order to identify the strut. A third method to reduce the minimum detectable lining thickness could involve the simultaneous acquisition of multiple images with different gains. These images could be combined to form a high

dynamic range image with no saturation, similar to the high dynamic range techniques used with conventional photography (Debevec and Malik 2007).

Excellent agreement for percent cellular coverage was found between the algorithm and the three observers for the ten volumetric datasets. The algorithm result was within one standard deviation of the coverages measured by the three observers for all BVMs except BVM 3 and 9. Nothing was noted to suggest why the algorithm differed from the average observational score for these particular mimics.

With a correlation coefficient of 89%, good agreement was observed between the BBI scores and the OCT percent cellular coverages. Low percentages are represented by scores in the 2–3 range and higher percentages are in the 3–4 range, with the highest percentage of 76% having a BBI score greater than 4. Imperfect correlation between the BBI scores and OCT percent cellular coverages may be partially attributed to the minimum thickness of tissue detected by OCT. For example, stent struts covered by a confluent lining with thickness less than the 30 μm would not be detected by the OCT algorithm but would be included in the BBI score.

In addition to the calculation of percent cellular coverage for an entire mimic, the algorithm also provided local coverage information on individual struts. The location and coverage status of strut-positive a-scans were recorded by the algorithm and later used to develop maps of the stent surface, as shown in figure 8. These maps may be useful for identifying regions that have not been covered by the cellular lining. A histological examination of human cadaver specimens suggested that the middle of drug-eluting stents is more likely to lack a neointimal lining than the distal and proximal ends of the stent (Finn *et al* 2007). These maps may help stent manufacturers identify properties that hinder endothelialization. Such properties may be geometric features or deployment characteristics of the struts. For example, Finn *et al* (2007) found the amount of endothelialization decreased as separation between stent struts became smaller.

Although this algorithm calculated percent cell coverage values in excellent agreement with the manual observations, several improvements can be made to the algorithm. Better strut identification performance could be obtained by taking advantage of the volumetric data. A strut identified in one image should be located at approximately the same position in the adjacent images of the volumetric dataset. Strut maps are an assessable way to check for erroneous strut identifications, since it provides a clear indication of the location of the stent struts. Any pixels in this mapping that do not conform to the expected strut pattern could be removed from analysis using a combination of median filtering, image erosion and dilation. A discontinuous region of a strut could be identified prompting a closer evaluation of that region using higher sensitivity algorithm parameters.

Both bulk percent cellular coverage and local strut coverage information were obtained for these stented blood vessel mimics. The software automatically calculates an estimate of the lining thickness covering each stent strut. Future versions of the algorithm could record and use these thicknesses to form stent maps showing the thickness of the cellular lining covering the struts.

The blood vessel mimic is a simplified model of a native artery. Application of this algorithm to *ex vivo* or *in vivo* studies of stented arteries may require modifications to the algorithm. Beyond the additional medial and adventitial layers, the native artery will have more microstructural elements that may complicate the analysis. In atherosclerotic plaques, these elements may include calcified regions and lipid pools. Despite these differences between mimics and native arteries, the metallic struts will still have the same visualization characteristics—a significantly bright reflection, dark shadow and concentrated intensity. The presence of these characteristics suggests that the strut identification algorithm should perform

well despite the additional complexity. The cell coverage algorithm depends only on a well-defined lumen and the bright reflection from the stent strut. Consequently, the cell coverage algorithms should be relatively insensitive to the additional tissue microstructure present beneath the neointima.

Future studies will be needed to assess the performance of this algorithm in stented arteries. Algorithm optimization could be performed with *ex vivo* arteries, where information from destructive techniques such as epi-fluorescence and histological analysis were available. The algorithm could then be extended to *in vivo* studies, where the performance of the algorithm could be further optimized if necessary based on manual analysis of OCT images. A study incorporating a diverse patient population would be required to determine whether a universal parameter set would be appropriate for all *in vivo* stented arteries.

7. Conclusion

The results from this study indicate that OCT can provide excellent visualization of the temporal response of blood vessel intimal surfaces to deployed stents, and that the automatic strut identification and cell coverage algorithms may be valuable tools in determining both endothelialization and re-cellularization of stents from volumetric OCT datasets. The algorithm provided percent cellular coverage measurements in excellent agreement with observational measures. The high sensitivity, specificity and percent correct classification measures suggest that these algorithms may be useful for rapid, accurate assessments of endothelialization to help guide new stent designs and drug treatments.

References

Bonnema G T, Cardinal K O, McNally J B, Williams S K and Barton J K 2007 Assessment of blood vessel mimics with optical coherence tomography *J. Biomed. Opt.* **12** 024018-1–6

Bouma B E *et al* 2003 Evaluation of intracoronary stenting by intravascular optical coherence tomography *Heart* **89** 317–20

Brezinski M E 2006 Optical coherence tomography for identifying unstable coronary plaque *Int. J. Cardiol.* **107** 154–65

Brezinski M E, Tearney G J, Weissman N J, Boppart S A, Bouma B E, Hee M R, Weyman A E, Swanson E A, Southern J F and Fujimoto J G 1997 Assessing atherosclerotic plaque morphology: comparison of optical coherence tomography and high frequency intravascular ultrasound *Heart* **77** 397–403

Buellesfeld L, Lim V, Gerckens U, Mueller R and Grube E 2005 Comparative endoluminal visualization of TAXUS crush-stenting at 9 months follow-up by intravascular ultrasound and optical coherence tomography *Z. Kardiol.* **94** 690–4

Cardinal K O, Bonnema G T, Hofer H, Barton J K and Williams S K 2006 Tissue-engineered vascular grafts as in vitro blood vessel mimics for the evaluation of endothelialization of intravascular devices *Tissue Eng.* **12** 3431–8

Debevec P E and Malik J 2007 Recovering high dynamic range radiance maps from photographs *SIGGRAPH97* pp 369–78

Farb A, Weber D K, Kolodgie F D, Burke A P and Virmani R 2002 Morphological predictors of restenosis after coronary stenting in humans *Circulation* **105** 2974–80

Finn A V, Joner M, Nakazawa G, Kolodgie F, Newell J, John M C, Gold H K and Virmani R 2007 Pathological correlates of late drug-eluting stent thrombosis: strut coverage as a marker of endothelialization *Circulation* **115** 2435–41

Fischman D L, Leon M B, Baim D S, Schatz R A, Savage M P, Penn I, Detre K, Veltri L, Ricci D and Nobuyoshi M (Stent Restenosis Study Investigators) 1994 A randomized comparison of coronary-stent placement and balloon angioplasty in the treatment of coronary artery disease *N. Engl. J. Med.* **331** 496–501

Iakovou I *et al* 2005 Incidence, predictors, and outcome of thrombosis after successful implantation of drug-eluting stents *JAMA* **293** 2126–30

Ito S, Itoh M and Suzuki T 2005 Intracoronary imaging with optical coherence tomography after cutting balloon angioplasty for in-stent restenosis *J. Invasive. Cardiol.* **17** 369–70

Konig A, Schiele T M, Rieber J, Theisen K, Mudra H and Klauss V 2002 Influence of stent design and deployment technique on neointima formation and vascular remodeling *Z. Kardiol.* **91** 98–102

Kume T, Akasaka T, Kawamoto T, Watanabe N, Toyota E, Sukmawan R, Sadahira Y and Yoshida K 2005 Visualization of neointima formation by optical coherence tomography *Int. Heart J.* **46** 1133–6

Masuda J, Terashima M and Yokoyama M 2001 Improved reproducibility of intravascular ultrasound assessment of coronary in-stent neointima with the use of an echogenic contrast agent *Jpn. Circ. J.* **65** 632–6

Matsumoto D, Shite J, Shinke T, Otake H, Tanino Y, Ogasawara D, Sawada T, Paredes O L, Hirata K and Yokoyama M 2007 Neointimal coverage of sirolimus-eluting stents at 6-month follow-up: evaluated by optical coherence tomography *Eur. Heart J.* **28** 961–7

Mintz G S, Hong M K, Raizner A E, Lee C W, Kim J J, Escolar E, Fearnot N E, Park S W, Park S J and Weissman N J 2005 Intravascular ultrasound assessment of neointima distribution and the length of stent that was free of intravascular ultrasound-detectable intimal hyperplasia in paclitaxel-eluting stents *Am. J. Cardiol.* **95** 107–9

Mourant J R, Freyer J P, Hielscher A H, Eick A A, Shen D and Johnson T M 1998 Mechanisms of light scattering from biological cells relevant to noninvasive optical-tissue diagnostics *Appl. Opt.* **37** 3586–93

Pfisterer M, Brunner-La Rocca H P, Buser P T, Rickenbacher P, Hunziker P, Mueller C, Jeger R, Bader F, Osswald S and Kaiser C 2006 Late clinical events after clopidogrel discontinuation may limit the benefit of drug-eluting stents: an observational study of drug-eluting versus bare-metal stents *J. Am. Coll. Cardiol.* **48** 2584–91

Salam A M, Al Suwaidi J and Holmes D R Jr 2006 Drug-eluting coronary stents *Curr. Probl. Cardiol.* **31** 8–119

Serruys P W, de Jaegere P, Kiemeneij F, Macaya C, Rutsch W, Heyndrickx G, Emanuelsson H, Marco J, Legrand V and Materne P (Benestent Study Group) 1994 A comparison of balloon-expandable-stent implantation with balloon angioplasty in patients with coronary artery disease. *N. Engl. J. Med.* **331** 489–95

Suzumura H, Suzuki T, Hosokawa H, Fukutomi T, Ito S and Itoh M 2002 Neointima in coronary stent does not increase during over 1-year in non-restenosed lesion at 6 months follow-up: serial volumetric intravascular ultrasound study *Japan. Heart J.* **43** 581–91

Takano M, Inami S, Jang I K, Yamamoto M, Murakami D, Seimiya K, Ohba T and Mizuno K 2007 Evaluation by optical coherence tomography of neointimal coverage of sirolimus-eluting stent three months after implantation *Am. J. Cardiol.* **99** 1033–8

Tanigawa J, Barlis P and Di Mario C 2007 Do unapposed stent struts endothelialise? In vivo demonstration with optical coherence tomography *Heart* **93** 378

Taylor A J, Gorman P D, Kenwood B, Hudak C, Tashko G and Virmani R 2001 A comparison of four stent designs on arterial injury, cellular proliferation, neointima formation, and arterial dimensions in an experimental porcine model *Catheter. Cardiovasc. Interv.* **53** 420–5